Nematic transitions in iron pnictide superconductors imaged with a quantum gas

Fan Yang[1,2,6], Stephen F. Taylor [1,2,6], Stephen D. Edkins[1,2,6], Johanna C. Palmstrom[1,3,4], Ian R. Fisher[1,3,4] and Benjamin L. Lev [1,2,5 ✉]

¹Department of Applied Physics, Stanford University, Stanford, CA, USA. ²E. L. Ginzton Laboratory, Stanford University, Stanford, CA, USA. ³Geballe Laboratory for Advanced Materials, Stanford University, Stanford, CA, USA. ⁴Stanford Institute for Materials and Energy Science, SLAC National Accelerator Laboratory, Menlo Park, CA, USA. ⁵Department of Physics, Stanford University, Stanford, CA, USA. ⁶These authors contributed equally: Fan Yang, Stephen F. Taylor, Stephen D. Edkins. ✉e-mail: benlev@stanford.edu

Nematic transitions in iron-pnictide superconductors imaged with a quantum gas

Fan Yang,[1, 2, *] Stephen F. Taylor,[1, 2, *] Stephen D. Edkins,[1, 2, *] Johanna C. Palmstrom,[1, 3, 4]
Ian R. Fisher,[1, 3, 4] and Benjamin L. Lev[1, 2, 5]

[1]*Department of Applied Physics, Stanford University, Stanford, CA 94305, USA*
[2]*E. L. Ginzton Laboratory, Stanford University, Stanford, CA 94305, USA*
[3]*Geballe Laboratory for Advanced Materials, Stanford University, Stanford, CA 94305, USA*
[4]*Stanford Institute for Materials and Energy Science, SLAC National Accelerator Laboratory,
2575 Sand Hill Road, Menlo Park, California 94025, USA*
[5]*Department of Physics, Stanford University, Stanford, CA 94305, USA*
(Dated: January 27, 2020)

A. Long-length-scale inhomogeneous birefringence

A variety of experimental probes are reported as having detected rotational C_4 symmetry breaking persisting tens of kelvin above the bulk structural transition temperature (as determined by scattering and thermodynamic probes) [1–7]. However, our local probes are consistent with the concurrent onset of resistivity anisotropy and twin-domain formation, at least where the domains walls do not wander; see Supp. Sec. B. To reconcile this apparent discrepancy, we now detail our observation of birefringence that is inhomogeneous on long-length-scales and persists to temperatures as high as 60-K above T_{nem}. These observations are consistent with the previous reports of C_4 symmetry breaking at $T > T_{\mathrm{nem}}$.

Supplemental Fig. 1 shows wide-area birefringence ($\theta(x, y)$) images for x = 0 and 2.5% samples at temperatures below, at, and above their respective T_{nem}. While short-length-scale birefringence modulations from twin-domains disappear above T_{nem}, long-length-scale, inhomogeneous birefringence persists up to 60-K higher.

Supplemental Figs. 1(d,h) show birefringence in the blue and orange boxes plotted versus temperature. Evident are the expected kinks in $|\theta(x, y)|$ due to the peak in nematic susceptibility near T_{nem}. Interestingly, the sign of $\theta(x, y)$ in the parent sample is the same in the two regions despite being morphologically consistent with orthogonally oriented domains. This might indicate the presence of a quenched lattice distortion from unintended strain along the same direction in both regions. That could cause the $\sim+0.2$-baseline shift we observe around which short and long-length-scale birefringence is modulated. Such a picture is also consistent with the observed peak, rather than dip, in the orange region's rotation, since the prevailing distortion axis would be co-aligned with that in the blue region.

We were not able to determine whether long-length-scale resistivity anisotropy is coincident with this birefringence due the currently limited field of view of the SQCRAMscope. Nevertheless, these observations suggest that the anisotropy observed by other probes [1–7] at $T > T_{\mathrm{nem}}$ may be the result of a large nematic susceptibility coupled to inhomogeneous unintended strain.

B. Additional scan of x = 2.5% sample

Supplementary Fig. 2(a,b) shows birefringence and measured magnetic field for scan region D3 of the x = 2.5% sample. The scan exhibits interesting features, highlighting the variety of domain morphology at the nematic transition. Limited magnetometry resolution blurs neighboring domains that otherwise appear distinct in optical birefringence. Birefringence measurements reveal the movement of domain walls near the transition temperature that can just be discerned in the lower-resolution magnetometry data, implying a bulk, rather than just near-surface effect. This movement, coupled with sensitivity and resolution limits, makes it difficult to compare the temperatures at which transitions in birefringence versus magnetometry occur in this scan. Rather than attempt to compare metrics like $A_B(T)$ and $A_\theta(T)$ for migrating domains of variable width, we instead simulate the magnetic field resulting from the domain structure in panel (a) and use it to compare with the actual magnetometry data in panel (b). To do so, we calculate the field we *would* detect if the birefringence structure in panel (a) were to faithfully serve as proxy for demarcating the bulk electronic nematic domain boundaries. The results are shown in panel (d), where the optical data have been convolved with the Biot-Savart kernel to account for finite resolution and noise from the sensitivity limit measured in Ref. [8] has been added; see below for simulation details.

Simulated magnetometry domains appear to be subsumed by noise above 97 K, nearly the same temperature at which the domains in magnetometry vanish outright or are also subsumed into detection noise. Because of this, we cannot tell if the magnetometry domains actually extend to higher temperatures, say, up to $\sim$100 K where the optical domains vanish. However, domains in the magnetometry data do seem to migrate just as in the simulation, showing that this is an effect of the bulk as well as the surface. Another complication is the broad

---

* F.Y, S.F.T., and S.D.E contributed equally to this work.
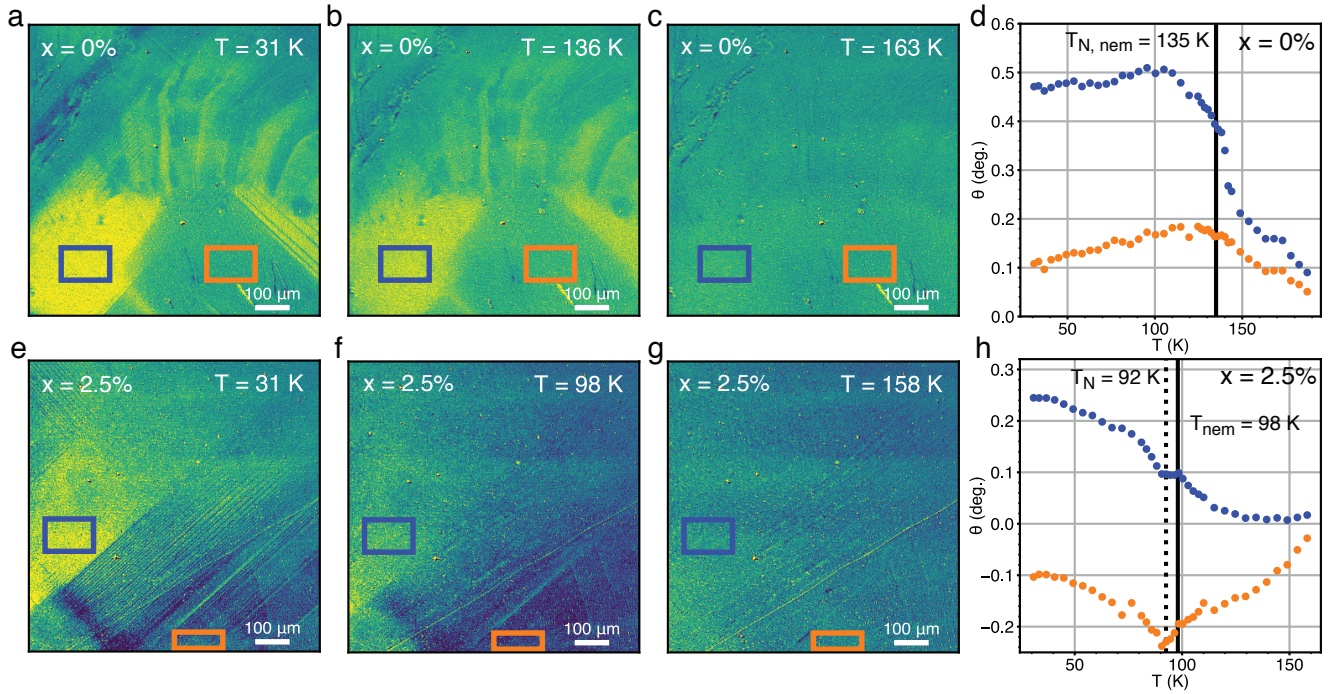
Supp. Fig. 1. Large-length-scale optical birefringence modulation. Data from x = 0% and 2.5%-doped samples in panels (a-d) and (e-h), respectively. Optical birefringence below the nematic transition (a,e), at the transition (b,f), and above the transition (c,g). (d,h) Polarization rotation angle as a function of temperature at two different regions marked by blue and orange rectangles in (a-c) and (e-g), respectively. Nematic and Néel transition temperatures are indicated by solid and dotted lines.
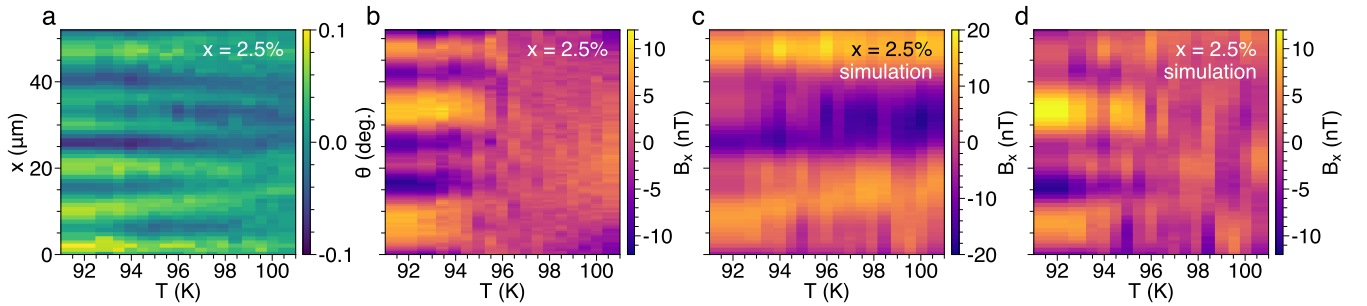
Supp. Fig. 2. Additional scan of the x = 2.5% sample in D3 region. Shown are (a) birefringence signal $\bar{\theta}(x,T)$, (b) magnetometry signal $\bar{B}_x(x,T)$, and (c) simulated magnetic field $\bar{B}_x^{\mathrm{sim}}(x,T)$ from the birefringence data in (a), and (d) simulated magnetic field with background subtracted $\bar{B}_x^{\mathrm{sim}}(x,T) - \bar{B}_x^{\mathrm{sim}}(x,T^*)$ $(T^* > T_{\mathrm{nem}})$.

magnetic feature of unknown origin that appears above ~ 97 K, which could also be masking the magnetic domain signal. The positive part of the feature is centered ± 15-μm about $x = 20$ μm, while negative wings emerge at the top and bottom of the scan. This feature is not evident in the optical measurement, though it is above the noise floor and presumably not a detection artifact.

We cannot discern whether domains in magnetometry vanish around 97 K due to detection noise or because they are subsumed into a broad magnetic feature of unknown origin. Thus, while we cannot be sure whether the x = 2.5% data is more consistent with a *single* nematic structural-electronic transition versus an extraor-

dinary surface transition scenario, the data do indicate that bulk and surface transitions differ by no more than few degrees and that strong short-length-scale nematic domains do not extend far above the expected bulk nematic transition temperature. Future magnetometry using a SQCRAMscope with improved resolution and sensitivity should help resolve what this feature is and exactly where the bulk transition lies in data where the domains migrate.

Simulation of expected magnetic field from optical rotation data

We will show in Supp. Sec. G that to leading order, the current density $j_y(x,y)$ is proportional to the resistivity anisotropy $1 - \rho_x/\rho_y$. Therefore, if we take the birefringence $\theta(x,y)$ as a proxy for nematicity, and by extension, resistivity anisotropy, then convolving it with the Biot-Savart kernel $G(k_x,k_y)$ gives the expected magnetic field $\bar{B}^{\mathrm{sim}}$; see Eq. (6) in Supp. Sec. F.

The raw and background-subtracted simulation results are shown in Supp. Figs. 2(c,d). We now detail the numerical procedure for generating the simulated field below. Supplemental Sec. G presents how to map measured current density to resistivity anisotropy. Briefly, the current density $j_y(x,y)$ perpendicular to the BEC is proportional, to leading order, to the resistivity anisotropy $1 - \rho_a/\rho_b$,

$$1 - \rho_a/\rho_b = \frac{2\delta j_y}{j_{\mathrm{bulk}}}, \tag{1}$$

where j_{bulk} is the applied bulk current density. Therefore, if we take the birefringence $\theta(x,y)$ as a proxy for nematicity, and by extension, resistivity anisotropy,

$$1 - \rho_a/\rho_b = \alpha\theta(x,y), \tag{2}$$

where α is an arbitrarily chosen conversion coefficient, then convolving δj_y with the Biot-Savart kernel $G(x,y)$ (see Supp. Eq. 6 in Supp. Sec. F) gives the expected magnetic field B_x^{sim}:

$$B_x^{\mathrm{sim}}(x,y) = j_y^{\mathrm{sim}}(x,y) * G(x,y) \tag{3}$$

$$= \frac{\alpha j_{\mathrm{bulk}}}{2}\theta(x,y) * G(x,y). \tag{4}$$

We note that the application of the aforementioned method to the data in Supp. Fig. 2(a) results in Supp. Fig. 2(c), which does not fully resemble the measured field shown in Supp. Fig. 2(b). However, by subtracting the simulated field at a higher temperature $T^* = 102.5\,\mathrm{K}$ from that of each temperature, we recover a field map Supp. Fig. 2(d) that is more similar to the measured field. This suggests that the long-length-scale birefringence reported in Supp. Sec. A might contribute an offset to the data observed here.

C. Sample preparation

Single crystals of $\mathrm{Ba(Fe_{1-x}Co_x)_2As_2}$, with nominal composition x = 0% and 2.5%, were grown using the self-flux technique described in Ref. [9]. The structural and Néel transition temperatures were determined from bulk resistivity measurements on crystals from the same growth batch following the procedure in Ref. [10]. The intra-batch variations in transition temperatures are typically $\sim 1\,\mathrm{K}$.

The crystals were cleaved and cut into thin rectangular plates, with edges of the crystal cut at roughly 45° to the tetragonal axis. The sizes of the crystals were measured using an SEM to be: $1.69\,\mathrm{mm} \times 2.35\,\mathrm{mm} \times 28\,\mathrm{\mu m}$ for the parent crystal, and $1.78\,\mathrm{mm} \times 2.23\,\mathrm{mm} \times 22\,\mathrm{\mu m}$ for the 2.5%-doped crystal. The variation in thickness is of the order 5–10 %. The crystals were positioned on lithographically patterned gold wires on the silicon wafer used to support the samples in the SQCRAMscope using a flip-chip bonder, and electrical contact between crystal and gold was made using silver epoxy.

D. Location of scan regions

The location of the scan regions P1, P2, D1, D2 and D3 referred to in the main text are indicated in Supp. Fig. 3.

E. Magnetometry measurement of bulk current density

In our calculations of resistivity anisotropy, we use a bulk current density j_{bulk} that is determined by dividing the total sample current by the cross-sectional area of the sample. This assumes that j_{bulk} is spatially homogeneous. To substantiate this assumption, we carried out a more direct local measurement of j_{bulk}, as we now explain. (The data listed below are taken from the parent compound as an example. Similar measurements carried out on the 2.5%-doped sample shows no discrepancy and are omitted here.) Due to the shape of our BEC trapping field, applying a magnetic field perpendicular to the BEC changes the distance between the sample surface and the BEC (which we refer to as the BEC height). The bulk sample current flows parallel to the BEC (along the x axis), which generates a perpendicular magnetic field (along the y axis). Thus, the BEC height reflects the mean current density $\bar{j}_{\mathrm{bulk}}$ in its vicinity.
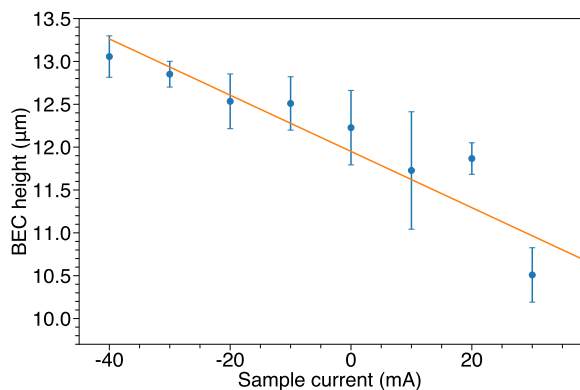
Starting with the BEC positioned about 10-μm away from the sample surface, we measured its height as a function of the total sample current, as shown in Supp. Fig. 4. We can determine the response of the gas height to the sample current to be $(-37 \pm 5)\,\mathrm{\mu m/A}$ in this example measurement. We then calibrated the response with external bias coils to find a coefficient of $(11 \pm 1)\,\mathrm{\mu m/G}$, from which we deduce that the sample generates a bias field near its surface with a field-per-current coefficient of $B_x/I = (3.4 \pm 0.5)\,\mathrm{G/A}$. Since the BEC height is much smaller than the lateral size of the sample, the field near the sample can be modelled by a thick infinite-sized slab conductor with current density j_y and magnetic field B_x given by

$$B_x = \frac{\mu_0 j_y h}{2} = \frac{\mu_0 I}{2w}, \tag{5}$$

where μ_0 is the vacuum permeability, h is the thickness of the sample, and w is the width of the sample. Given the
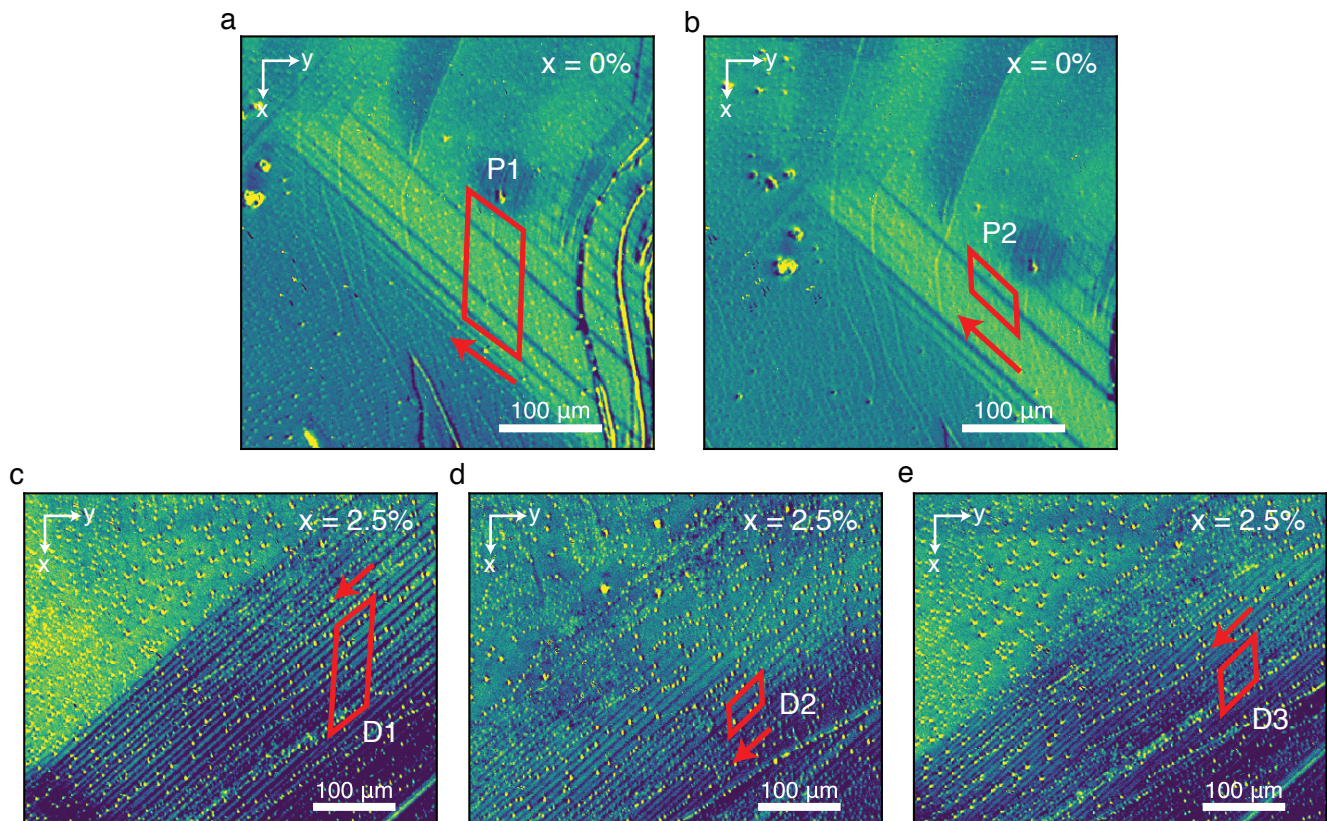
Supp. Fig. 3. SQCRAMscope magnetometry scan regions. The scan regions P1 and P2 are indicated by red parallelograms on $\theta(x, y)$ images for parent $BaFe_2As_2$ in panels (a–b). The regions D1-3 are similarly indicated for 2.5% Co-doped $Ba(Fe_{1-x}Co_x)_2As_2$ in panels (c–e). Red arrows indicate the direction of the scan. The speckles seen on the sample surfaces were likely introduced post-growth via accidental ablation of glue. They do not have a noticeable effect on electronic transport.

a spatially uniform distribution.

F. Extracting current density from magnetic field
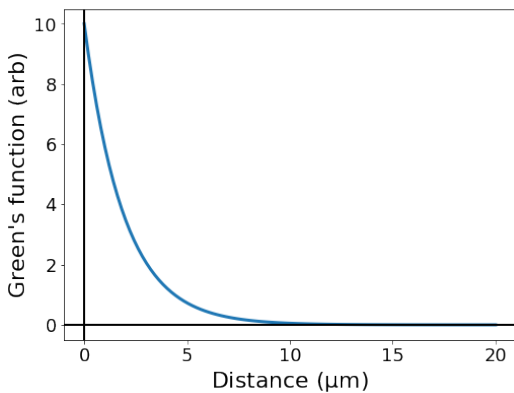
We describe the method used to extract current density $j_y(x, y)$ from the magnetic field $B_x(x, y)$ measured using the SQCRAMscope. This method expands upon that detailed in Ref. [8]. Assuming an infinite sheet of electric current that is uniform along its thickness h, the Green's function for the Biot-Savart kernel $G(k_x, k_y)$ used to compute the field a distance r from the surface of the sheet is given by

$$G(k_x, k_y) = \mu_0 \sinh\left(h\bar{k}/2\right) \exp\left[-\bar{k}(d + h/2)\right]/\bar{k}, \quad (6)$$

where $\bar{k} \equiv \sqrt{k_x^2 + k_y^2}$ is the spatial wavenumber. The y-component of the current density j_y is computed by deconvolution with the Biot-Savart kernel, or equivalently by division in Fourier space:

$$j_y(k_x, k_y) = B_x(k_x, k_y)/G(k_x, k_y). \quad (7)$$

The Green's function for an infinitesimally thin sheet of current a depth d within the sample decays exponentially with length scale $1/\bar{k}$. Thus, spatial frequencies

Supp. Fig. 4. BEC height versus sample current. Error bars represent standard error of the mean.

sample dimensions listed in Supp. Sec. A, we expect a field-per-current coefficient of $3.7\,\text{G/A}$, in agreement with the BEC-height measurements. This shows that the local j_{bulk} at the location we perform our magnetometry does not deviate substantially from that calculated assuming

Supp. Fig. 5. Green's function versus depth below sample surface for a 12-μm spatial wavelength roughly corresponding to the observed domain length scale.

corresponding to $12\,\mu m$, for example, which close to the width of a typical domain in our samples, have a decay length of $1/\bar{k} = 2\,\mu m$ within the bulk. Supplementary Fig. 5 plots the Green's function versus depth below the sample surface for this spatial frequency. It shows that magnetometry is primarily sensitive to the top few microns of sample current when detecting signals with spatial extent matched with the typical domain size. In contrast to the 30-nm penetration-depth scale of the optical measurements, this corresponds to bulk length scales.

The convolution method described above is mathematically exact, but also extremely sensitive to high-frequency noise due to the exponential term in Eq. (6) unless $\Gamma \equiv (d \pm h/2)\max(\bar{k}) \ll 1$. In the present work $\Gamma \approx 300$. Thus, we must suppress high frequencies with an appropriately chosen window function. We use a Hanning window,

$$H(\bar{k}) = \begin{cases} \cos^2 \frac{\bar{k}}{2\lambda} & \bar{k} \leq 2\pi/\lambda, \\ 0 & \bar{k} > 2\pi/\lambda \end{cases}, \qquad (8)$$

with a cut-off that removes all frequencies greater than $2\pi/\lambda$. The value of λ should be chosen large enough to not filter out critical frequency components of the signal, but not so large as to allow excessive amounts of noise to corrupt the signal. This number will set the effective spatial resolution of the SQCRAMscope for imaging current density, down to a limit no smaller than the spatial resolution for magnetic field imaging (presently $2.2\,\mu m$ with the lens system being used) [8]. For the 2D current density plots in Figs. 2 (g) and (h), the large thickness of the samples requires a relatively large value of λ to adequately suppress high-frequency noise. We choose $\lambda = 8\ \mu m$, resulting a FWHM point-spread resolution of $8\,\mu m$ when imaging current density in these samples. The 8-μm cutoff is chosen to minimize the amplified noise without significantly reducing the size of the measured signal in any but the smallest of domains; $8\,\mu m$ is close to the width of the narrowest domains imaged in Figs. 2.
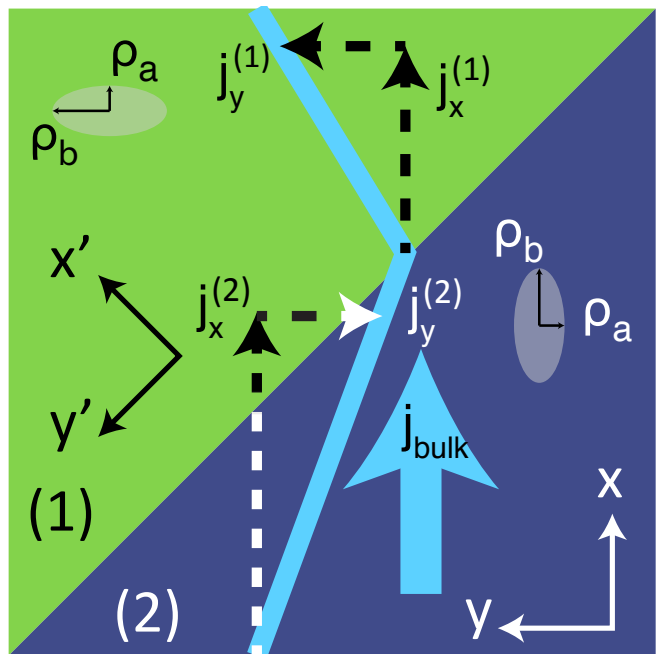
Supp. Fig. 6. Domain structure for theoretical calculation of anisotropy.

G. Model relating current density to resistivity anisotropy

This section describes the derivation of an expression for resistivity anisotropy. An analytic model is used to relate resistivity anisotropy to current density. We then use this model in Supp. Sec. H to calculate resistivity anisotropy from measured current density.

Consider an infinite conductor in a 2D plane representing a crystal in the orthorhombic phase. A single, infinitely long domain wall extends through the crystal at 45° to the x and y axes, as shown in Supp. Fig. 6. In the upper domain, denoted (1), the a and b crystal axes are parallel to the x and y coordinate axes, respectively, while in the lower domain, denoted (2), the situation is reversed: a is parallel to y and b is parallel to x. In each domain, the resistivity takes a value ρ_a along the crystal a axis and ρ_b along the b axis.

In this model, current is driven along the x direction, and the current flow is deflected at the domain boundary by the anisotropic resistance to give a finite current density in the y direction. Let $j_x^{(1)}$, $j_x^{(2)}$, $j_y^{(1)}$, and $j_y^{(2)}$ refer to current densities in the x and y directions in either the first or second domain region, as denoted by the superscript. We can experimentally measure the difference in current along the y direction in the two domains

$$\delta j_y \equiv j_y^{(2)} - j_y^{(1)}. \qquad (9)$$

We treat all other current densities, as well as the resistivities, as unknown, and gather a set of equations that will let us solve for the ratio of resistivities, $1 - \rho_a/\rho_b$.

Two relations can be obtained by conservation of charge and Faraday's law. These give, respectively, $\nabla \cdot \vec{j} = 0$ and $\nabla \times \vec{E} = 0$, where $\vec{E}$ denotes the electric field. Taking a divergence and line integral, respectively, across a long, narrow box straddling the domain boundary, we can convert these differential equations to simple forms. Defining the coordinates x' (y') to be perpendicular (parallel) to the domain wall, we write the result of these integrals as:

$$j_{x'}^{(1)} = j_{x'}^{(2)} \tag{10}$$

$$E_{y'}^{(1)} = E_{y'}^{(2)}. \tag{11}$$

Converting back to the $x - y$ coordinate system and inserting the constitutive equation $E_i = \rho_{ij} j_j$, we arrive at the following equations:

$$j_x^{(1)} + j_y^{(1)} = j_x^{(2)} + j_y^{(2)} \tag{12}$$

$$-\rho_a j_x^{(1)} + \rho_b j_y^{(1)} = -\rho_b j_x^{(2)} + \rho_a j_y^{(2)}. \tag{13}$$

We now obtain a final set of two equations by inserting assumptions about the net flow of current. To obtain a more general result, we allow for the two domains to be of unequal size, letting a fraction f_1 of the sample be domain 1 and a fraction f_2 be domain 2, where $f_1 + f_2 = 1$. We assume there is a net current density j_{bulk} in the x direction, and no net current in the y direction, representing our current supply driving electronic transport through the crystal. By averaging the x current over a line parallel to the y axis, while averaging the y current over a plane parallel to the x axis, we obtain:

$$f_1 j_x^{(1)} + f_2 j_x^{(2)} = j_{\text{bulk}} \tag{14}$$

$$f_1 j_y^{(1)} + f_2 j_y^{(2)} = 0. \tag{15}$$

We can now solve this set of equations for $1 - \rho_a/\rho_b$ in terms of δj_y, j_{bulk}, f_1, and f_2. First, we take Eq. (9) and Eq. (15), which combine to give:

$$j_y^{(1)} = -f_2 \delta j_y \tag{16}$$

$$j_y^{(2)} = f_1 \delta j_y. \tag{17}$$

Substituting these into Eq. (12) and Eq. (14), we solve for $j_x^{(1)}$ and $j_x^{(2)}$:

$$j_x^{(1)} = j_{\text{bulk}} + f_2 \delta j_y \tag{18}$$

$$j_x^{(2)} = j_{\text{bulk}} - f_1 \delta j_y. \tag{19}$$

Finally, we substitute the above into Eq. (13):

$$-\rho_a \left(j_{\text{bulk}} + f_2 \delta j_y \right) - \rho_b f_2 \delta j_y = \tag{20}$$

$$-\rho_b \left(j_{\text{bulk}} - f_1 \delta j_y \right) + \rho_a f_1 \delta j_y. \tag{21}$$

Simplifying, we obtain:

$$\rho_a/\rho_b = \frac{j_{\text{bulk}} - \delta j_y}{j_{\text{bulk}} + \delta j_y}. \tag{22}$$

We can then rewrite this as

$$1 - \rho_a/\rho_b = \frac{2\delta j_y}{j_{\text{bulk}} + \delta j_y}. \tag{23}$$

This equation provides the resistivity anisotropy as a function of only the known bulk current density j_{bulk} and the measured current density δj_y. Note that this equation is also independent of the relative size of the domains, as the geometric factors f_1 and f_2 do not appear in the result.

To verify the validity of this equation, we performed finite element simulations of electric current flowing through adjacent domains. The domains have alternating anisotropic resistance and varying widths, similar to the domain patterns we see in the measured $\text{Ba(Fe}_{1-\text{x}}\text{Co}_\text{x})_2\text{As}_2$ crystals. Equation (1) correctly determined the anisotropy in these models to within numerical error of a few percent, and did so consistently for a variety of domain widths and anisotropy magnitudes.

H. Computation of resistivity anisotropy from magnetic field

We now detail the use of the model described above in Supp. Sec. G to compute the temperature dependence of the resistivity anisotropy from the measured magnetic field B_x. To compute the resistivity anisotropy using Eq. (1), one must first calculate the current density j_y. While the deconvolution method detailed in Supp. Sec. F calculates j_y from B_x using minimal assumptions about the spatial structure of j_y, it is susceptible to making a biased estimate of the j_y modulation amplitude due to the need to choose a low-pass filter cut-off frequency. In Fig. 2 of the main text we establish, using the deconvolution method, that the domain structure exhibited in j_y is in good correspondence with that in the birefringence. Thus, the birefringence signal provides prior knowledge of j_y that may be used to make an estimate of j_y from B_x that is less susceptible to bias.

Rather than computing j_y by direct deconvolution of B_x, we use an iterative method. Using birefringence images, we construct a parametric model of j_y which is then convolved with the Biot-Savart kernel Eq. (6) to yield a trial magnetic field B_x'. We then vary the model parameters by gradient descent so as to minimize the residual squared error (RSE) between B_x' and the measured magnetic field B_x. The amplification of high-frequency noise discussed in Supp. Sec. F is avoided because this method does not directly deconvolve magnetic field data. The peak-to-peak amplitude of j_y, a model parameter, can then be used to compute anisotropy as described in Supp. Sec. G.

As shown in Supp. Fig. 7, we model j_y as being of fixed magnitude but rapidly reversing polarity upon crossing
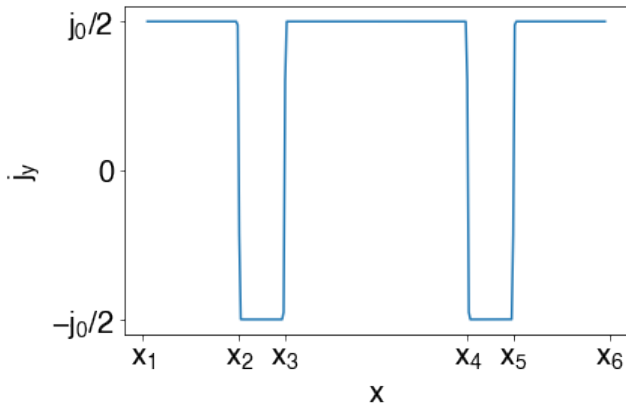
Supp. Fig. 7. Example of current density model used to fit magnetic field data.

a domain wall. We parameterize this model according to

$$j_y(x, j_0, \epsilon, x_1, \ldots, x_N) = \sum_{i=1}^{N} (-1)^i j_0 \left[\text{erf}([x - x_i]/\epsilon) + 1 \right]/2,$$
(24)

where j_0 is the amplitude of the current; the x_i define the positions of the domain walls, and $\epsilon \to 0$ such that the error function approximates a step function.

The trial magnetic field B_x' is computed as the convolution of $j_y(x, j_0, x_1, \ldots, x_N)$ with the Biot-Savart Green's function G:

$$B_x'(x, j_0, x_1, \ldots, x_N, B_0, B_1) = G * j_y(x, \epsilon, x_1, \ldots, x_N)$$
$$+ B_0 + B_1 x + B_2 x^2, (25)$$

where B_0, B_1, and B_2 account for fields produced by large-length-scale current modulations near the region of interest. Choosing a temperature where the magnetic signal is near its strongest, we determine the position of the domain walls by minimizing the RSE between B_x' and B_x by varying j_0, x_i, B_0, and B_1. We then constrain the x_i such that the spacing between domain walls is fixed but they may undergo a rigid translation and the position of the domain walls is determined by a single fit parameter x_0. To determine the temperature dependence of j_y we use the trial magnetic field

$$B_x'(x, j_0, x_0, B_0, B_1) = G * j_y(x, \mu, x_1 + x_0, \ldots, x_N + x_0)$$
$$+ B_0 + B_1 x + B_2 x^2, \qquad (26)$$

to find the j_0, x_0, B_0, B_1, and B_2 that minimize the RSE in magnetic field. We can then use Eq. (1) to compute the resistivity anisotropy at each temperature by setting $\delta j_y = j_0$.

We estimate the uncertainty in current density by comparing the measured magnetic field to that calculated using the current density model and its optimal set of parameters. Supplementary Figs. 8 (a) and (b) show typical measured (orange) and model (blue) magnetic field for the parent and 2.5%-doped samples, respectively. We

take the difference of these two curves and deconvolve the result with the Biot-Savart kernel, following the procedure in Supp. Sec. F with a cutoff frequency of 8 μm. The resulting current density represents an estimate of the difference between our model current density and the current density flowing through the sample. We overlay in Supp. Fig. 8 (c) and (d) for the parent and 2.5%-doped samples, respectively, the model (blue) and error (red) current densities for the same data presented in (a) and (b).

We define the uncertainty in δj_y to be the spatial standard deviation in the computed error current density added in quadrature with error resulting from a 10% variation in sample thickness. The resistivity anisotropy error bars in Figs. 3 (e) and (f) result from propagating these uncertainties through Eq. (1). These error bars represent uncertainty due to both random sources (e.g., noise in the measurement) and systematic sources, such as a specification of the current density model.

I. Definition of domain-averaged amplitudes

We now provide the definitions for the domain-averaged amplitudes $A_B(T)$ and $A_\theta(T)$ used in the main text. We define the domain-averaged amplitude for magnetometry and birefringence modulations to be

$$A_B(T) = \underset{\alpha}{\text{argmin}} \left\{ \int \mathrm{d}x \left[\bar{B}_x(x, T) - \alpha \bar{B}_x(x, T_{\text{ref}}) \right]^2 \right\}$$
(27)

and

$$A_\theta(T) = \underset{\beta}{\text{argmin}} \left\{ \int \mathrm{d}x \left[\bar{\theta}_x(x, T) - \beta \bar{\theta}_x(x, T_{\text{ref}}) \right]^2 \right\},$$
(28)

respectively. T_{ref} is a reference temperature chosen to be that where the amplitude of spatial modulations associated with domains is largest. We expect the domain amplitude to decrease from a peak value near 1 down to 0 as temperature rises through T_{nem}. The domain-averaged amplitude will predominately reflect the size of features that are large in amplitude or extent. Smaller or unresolved features will therefore have a minimal effect on the amplitude, and the presence of, e.g., narrow domains that are visible in birefringence but not visible in magnetometry, will not negatively impact the efficacy of this technique.

J. Simulation of magnetic field for Figure 1d

We simulated the magnetic field we expect to measure in a two-step process. First, the current density for a given configuration of nematic domains was computed using finite-element analysis. This current density was then used to numerically compute the magnetic field by convolution with the Biot-Savart kernel; see Supp. Sec. F.
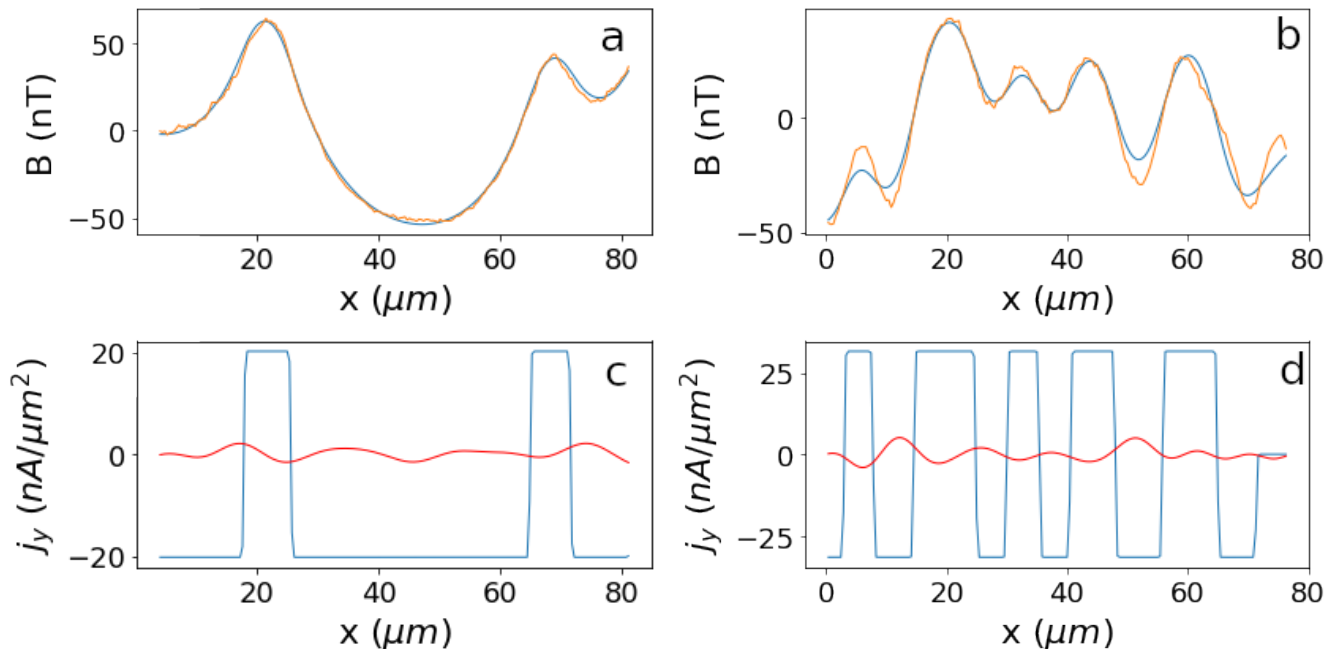
Supp. Fig. 8. Error estimation. Panels (a) and (b) show the typical measured magnetic field (orange) and the magnetic field that results from the optimized current density model (blue) for the parent and doped samples, respectively. Panels (c) and (d) show the optimized current density (blue) and current density error (red) produced by deconvolving the difference in measured and calculated magnetic field in panels (a) and (b).

K. Birefringence measurements

We augmented our SQCRAMscope magnetometer with an optical birefringence microscope similar to the setup in [11]; see Supp. Fig. 9. The sample, mounted on a silicon substrate in a UHV chamber, is illuminated by a 780-nm LED with polarization set by a linear polarizer and a $\lambda/2$ waveplate. Light reflected from the sample passes through another linear polarizer and is imaged onto a CCD camera. Silver-coated mirrors and a 50:50 plate beamsplitter are carefully chosen to minimize distortion of the polarization, giving rise to an extinction ratio in excess of 1:1000. This provides an angular resolution better than 0.1°. The imaging optics are specifically designed to be installed in the SQCRAMscope with in-vacuum lenses to provide better numerical aperture. The microscope was tested with a 1951 USAF target and found to have a spatial resolution of ~ 3 μm, estimated using the Rayleigh criterion.

The microscope determines the polarization rotation of light reflected from the sample using the two nearly crossed polarizers. The intensity of the light on the CCD camera is therefore indicative of the rotation angle $\Delta\theta = \theta_{\text{out}} - \theta_{\text{in}}$, where θ_{in} is the linear polarization angle of the incident light and θ_{out} is that of the reflected light. For samples discussed in the main text, the largest signal is found when the incident light is linearly polarized along the orthorhombic $(110)_o$ direction. This is consistent with the breaking of C_4 symmetry resulting
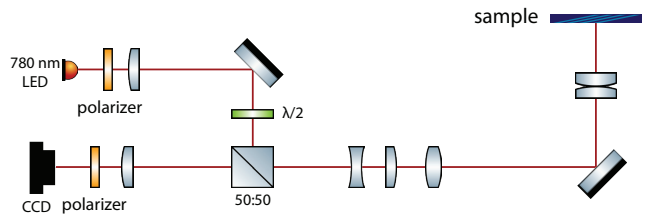
Supp. Fig. 9. Polarimeter schematic for optical birefringence measurements.

in a reflectance difference between light polarized along $(100)_o$ versus $(010)_o$. Therefore, we fix the incident polarization to be at 45° with respect to the orthorhombic axes, and define it to be the angular origin throughout the paper, i.e., $\theta_{\text{in}} = 0$ and $\theta_{\text{out}} = \Delta\theta$.

Because only a small optical birefringence is exhibited by $\text{Ba}(\text{Fe}_{1-x}\text{Co}_x)_2\text{As}_2$, even in the orthorhombic state, care must be taken to observe a signal. Depending on whether high accuracy or precision is required, we choose to operate the optical birefringence microscope in one of two imaging modes.

The first mode, which we call the relative mode, enables precise measurements of the relative polarization rotation angle between points on the sample $\Delta\theta(\vec{r}_1) - \Delta\theta(\vec{r}_2)$ at the expense of an overall angular offset. For a given location on the sample, the intensity recorded on

the camera is

$$I(x, y; \alpha) \propto \sin^2[\alpha - \Delta\theta(x, y)], \qquad (29)$$

where we denote the angle of the second polarizer (the analyzer) measured from the maximum extinction position in the absence of birefringence α. By recording images at a series of α values, $\Delta\theta$ is extracted through a least-square fit to $I(\alpha)$. However, we note that the accuracy of $\Delta\theta$ is limited by that of α, which is set by the precision of optical components and is on the order of $0.2°$. Consequently, small $\Delta\theta$ cannot be directly compared against zero to infer the sign of polarization rotation. This mode of operation is suitable for measuring the contrast between twin domains, and therefore was employed for the data shown in Figs. 2–4.

The second mode, which we call the absolute mode, obviates this problem by fixing the angle of the analyzer α during sample cool-down and warm-up. This provides an improved accuracy in angle measurements but suffers from reduced precision. In this operation mode, a differential image is constructed as

$$\begin{aligned} \Delta I(x, y) &= I(x, y; \alpha_+) - I(x, y; \alpha_-) \\ &\propto \sin^2(\alpha_+ - \Delta\theta) - \sin^2(\alpha_- - \Delta\theta) \\ &\approx (\alpha_+^2 - \alpha_-^2) - 2(\alpha_+ - \alpha_-)\Delta\theta(x, y), \quad (30) \end{aligned}$$

where α_- and α_+ are the angles of the analyzer during cool-down and warm-up, respectively. Here, the previous uncertainty in α is replaced by the unknown but fixed proportionality factor $\Delta\theta(x, y)$ across datasets. We are therefore able to compare the rotation angle directly to zero and thus identify domains of opposite sign in the nematic order parameter. In addition, with a reference dataset taken in the relative mode, we are able to calibrate-out the unknown proportionality factor. This results in the dataset shown in Supp. Fig. 1, where the birefringence of both parent and 2.5%-doped samples is measured across a large temperature span, all while retaining angular resolution in absolute units.

L. Registration of optical birefringence and magnetometry images

The optical birefringence and the magnetometry scans are performed using different optical axes and imaging systems. To remove this spatial offset of the birefringence images to the magnetometry maps, we introduce a linearly polarized 780-nm laser beam resonant with the ^{87}Rb D2 transition along the same path as the polarimetry light source (see white beam in Fig. 1) and perpendicular to the sample surface. Absorption images of the BEC are then collected on the birefringence imaging camera. The same BEC is also imaged through the SQCRAMscope imaging axis (see red beam in Fig. 1). Together with the known magnification of the two imaging systems, this allows us to construct the coordinate transformation that brings the magnetometry data into the same coordinate system as the birefringence images. In particular, we take images of the samples with the birefringence imaging camera immediately after taking each BEC absorption image on the SQCRAMscope imaging axis. An up-sampled DFT cross-correlation-based image registration algorithm [12, 13] is used to register the optical sample images so as to reconstruct the magnetometry scan regions on the sample plane. This provides us with the ability to make a direct comparison between the two modes of operation, as shown in Figs. 2–4 of the main text. We further apply the cross-correlation method between datasets taken at different temperatures to align features seen in magnetometry of Figs. 2 and 4.

M. Trap parameters

The atomic cloud utilized by the SQCRAMscope is confined by a magnetic Ioffe-Pritchard trap as described in previous work [8]. In the present work, the longitudinal and transverse magnetic traps have typical frequency (12.2 ± 0.2) Hz and (1.41 ± 0.05) kHz, respectively. In addition, a uniform 0.3 mT bias field provides an atomic quantization axis along $\hat{x}$. The trap is positioned 2.3 ± 0.4-μm below the surface of the sample. The atoms could be positioned as close as 800 nm [8], limited by trap width, but we choose a large distance in this work for ease of use.

The magnetic field experienced by the sample due to the magnetic trap is close to the 0.3-mT trap bias field near the atomic cloud, and increases to a maximum value of less than 10 mT at the edge of the sample farthest from the atoms. Magnetic fields of these small magnitudes are expected to have a negligible effect on the sample's resistivity and transition temperature [14].

[1] Thewalt, E. *et al.* Imaging anomalous nematic order and strain in optimally doped BaFe$_2$(As, P)$_2$. *Phys. Rev. Lett.* **121**, 027001 (2018).

[2] Stojchevska, L., Mertelj, T., Chu, J. H., Fisher, I. R. & Mihailovic, D. Doping dependence of femtosecond quasiparticle relaxation dynamics in Ba(Fe,Co)$_2$As$_2$ single crystals: Evidence for normal-state nematic fluctuations. *Phys. Rev. B* **86**, 024519 (2012).

[3] Shimojima, T. *et al.* Pseudogap formation above the superconducting dome in iron pnictides. *Phys. Rev. B* **89**, 045101 (2014).

[4] Sonobe, T. *et al.* Orbital-anisotropic electronic structure

in the nonmagnetic state of $BaFe_2(As_{1-x}P_x)_2$ superconductors. *Sci. Rep.* **8**, 2169 (2018).

[5] Yi, M. *et al.* Symmetry-breaking orbital anisotropy observed for detwinned $Ba(Fe_{1-x}Co_x)2As_2$ above the spin density wave transition. *Proc. Natl. Acad. Sci. U.S.A.* **108**, 6878–6883 (2011).

[6] Iye, T. *et al.* Emergence of orbital nematicity in the tetragonal phase of $BaFe_2(As_{1-x}P_x)_2$. *J. Phys. Soc. Jpn.* **84**, 043705 (2015).

[7] Kasahara, S. *et al.* Electronic nematicity above the structural and superconducting transition in $BaFe_2(As_{1-x}P_x)_2$. *Nature* **486**, 382–385 (2012).

[8] Yang, F., Kollár, A. J., Taylor, S. F., Turner, R. W. & Lev, B. L. Scanning quantum cryogenic atom microscope. *Phys. Rev. Appl.* **7**, 034026 (2017).

[9] Chu, J.-H., Analytis, J. G., Kucharczyk, C. & Fisher, I. R. Determination of the phase diagram of the electron-doped superconductor $Ba(Fe_{1-x}Co_x)_2As_2$. *Phys. Rev. B* **79**, 014506 (2009).

[10] Chu, J.-H. *et al.* In-plane resistivity anisotropy in an underdoped iron arsenide superconductor. *Science* **329**, 824–826 (2010).

[11] Tanatar, M. A. *et al.* Direct imaging of the structural domains in the iron pnictides AFe_2As_2(A=Ca,Sr,Ba). *Phys. Rev. B* **79**, 180508 (2009).

[12] Padfield, D. Masked Object Registration in the Fourier Domain. *IEEE Transactions on Image Processing* **21**, 2706–2718 (2012).

[13] Guizar-Sicairos, M., Thurman, S. T. & Fienup, J. R. Efficient subpixel image registration algorithms. *Optics Letters* **33**, 156–158 (2008).

[14] Chu, J.-H. *et al.* In-plane electronic anisotropy in underdoped $Ba(Fe_{1-x}Co_x)_2As_2$ revealed by partial detwinning in a magnetic field. *Phys. Rev. B* **81**, 214502 (2010).